Session PR-3

Packaging Reliability(3)

The Striated Deformation of Sn Solders under High Frequency Resonant Vibration
C. M. CHUANG, T. S. LUI, L. H. CHEN, National Cheng-Kung University, Taiwan

Reliability Evaluation of Semiconductor using Ultrasound
Hyoseong JANG, Sonix Korea, Korea
Job HA, Kyungyoung JHANG, Hanyang University, Korea
Joonhyun LEE, Pusan National University, Korea

Study on Residual Stress in Viscoelastic Thin Film using Curvature Measurement Method
Y. T. IM, J. H. KIM, S. T. CHOI, Korea Advanced Institute of Science and Technology, Korea

The Striated Deformation of Sn solders under High Frequency Resonant Vibration

C. M. Chuang, T.S. Lui and L.H. Chen
Department of Materials Science and Engineering,
National Cheng-Kung University, Tainan, 701 Taiwan, ROC
E-mail: Snail@cubic.mat.ncku.edu.tw or z7408020@email.ncku.edu.tw

Abstract

A striated deformation feature was found commonly in solders during vibration test. This deformation evidence will be promoted under resonant vibration when the Sn-rich phase with a coarse size or the specimens with a longer vibration cycles. For Sn-Pb solders, the occurrence of striated deformation tend to generate fine intergranular cracks that will promote the crack propagation and the formation of main crack. On the other hand, for lead-free Sn-Zn and Sn-Ag solders, the striated deformation virtually plays an important role in absorbing the vibration energy and lead to an improvement of the vibration fracture resistance.

I. Introduction

Sn-Pb solders have been widely used in electronic components. Pb, however, damages the environment and presents a hazard to human health, so prohibition of the use of Pb in solder is immanent[1,2]. A great amount of research works, therefore, has aimed to develop suitable lead-free solders[3,4]. The Sn-Zn eutectic solder whose melting point (472K) is close to the Sn-Pb eutectic solder and possesses good mechanical strength. Besides, the Sn-Ag solders have good shear strength, creep resistance, thermomechanical fatigue behavior and wetting reliability on copper and copper alloys. But the major problem of Sn-Ag eutectic solders for displacement Sn-Pb eutectic solder is working temperature. Its eutectic melting point (494K) is higher than Sn-Pb eutectic solder. Presently, the development of lead-free solders based on Sn-Zn and Sn-Ag alloys appear to have significant potential.

On the other hand, when these electronic components with solder joints are assembled in dynamic machines e.g., vehicles, failure may occur due to vibrational cyclic loading. The failure rate will be accelerated especially when the vibration frequency suffers the resonant frequency, a specific natural frequency of materials[5,6]. The frequency of traditional fatigue studies is below 1Hz, does not satisfy to acquaint the deformed behaviors of solders under vibration.

This study aimed on the vibration fracture problems of solders, according to our previous studies[7~9], a striated deformation evidence could be observed in Sn-rich phase under high frequency vibration state (~10^2 Hz), that significantly affect the vibration fracture behaviors solders. The onset conditions and the effects of this deformation behavior on vibration fracture still should be clarified, for the purpose to verify the reliability of Sn-Pb solders and lead-free solders under vibration.

II. Experimental Procedure

A. Materials preparation

Two Sn-Pb solders, two Sn-Zn solders and one Sn-Ag solder were prepared. All melts were cast into a 4.2mm-thick Y-shaped chill graphite mold[7], individually. Table 1 lists the major chemical composition, melting and pouring conditions. According to the weight percentage of second element, two Sn-Pb alloys were named Sn-30Pb and Sn-40Pb, the other two Sn-Zn alloys were named Sn-7Zn and Sn-11Zn, and another the Sn-3.5wt% Ag sample was named Sn-3.5Ag.

After cast, all materials were machined for resonant vibration specimens. Two notched-shape specimens (V-notched and U-notched) were prepared and the dimension was shown in Fig. 1(b) and (c). Before vibration testing, all most specimens were stabilized with following conditions: (Sn-Pb system: 373K for 1 hr, Sn-Zn system: 393K for 1 hr, and Sn-3.5Ag: room temperature > 240 hr) and some V-notched Sn-40Pb samples were treated at 423K for 16hrs to enlarge the grain size (named Sn-40Pb C).

B. Vibration testing

The vibration setup is shown in Figure 1(a). Each test specimen was clamped on its notched end to a vibration shaker, with the other end equipped with a deflection sensor to measure the deflection amplitude. Vibration frequency and the push force of the shaker were generated through a vibration controller. The testing process and the quantitative analysis of vibration characteristics could refer to our previous studies[7~9].

Table 1 Chemical composition (wt%) and pouring conditions of experimental materials

	Pb	Zn	Ag	Sn	Pouring temp. (K)	Mold temp. (K)
Sn-30Pb	29.8	—	—	Bal.	558	453
Sn-40Pb	39.7	—	—	Bal.	543	423
Sn-7Zn	—	6.7	—	Bal.	563	423
Sn-9Zn	—	9.2	—	Bal.	563	423
Sn-3.5Ag	—	—	3.5	Bal.	583	453

Table 2 Vibration frequency and shaker push force of experimental material under the identical initial deflection of 2.4mm

	Sn-30Pb	Sn-40Pb	Sn-7Zn	Sn-9Zn	Sn-3.5Ag
Vibration Frequency (Hz)	70±1	69±1	73±1	73±1	72±1
Push Force (G)	2.9±0.1	2.6±0.1	3.0±0.1	3.4±0.1	3.4±0.2

Deformation as well as crack propagation was observed in SEM after the vibration test. The crack propagation length was measured as the value of the projected crack length, which can be defined as the length of the projection from the main crack to the direction of applied normal force (i.e., direction of linking both notches of the sample).

C. The onset conditions of striated deformation

First, two notched-shape stabilized Sn-40Pb specimens were used to explore the effect of cyclic number. Due to the propagation rate of main crack is the major reason that determines the deteriorating rate of specimens. In V-notched specimens, the main crack initiated at the initial testing stage and propagated with increasing cyclic number, therefore, the V-notched specimen deteriorates faster and the time that the deflection amplitude keeping in resonant state is shorter. On the other hand, in U-notched specimens, the main cracks initiated when the testing approaches the final vibration stage (the deflection amplitude will descent). So, the deflection amplitude of U-notched specimens could keep in resonant state more cycles. However, there are one more main cracks occurrence at the notch and the location of main crack is unsure, the U-notched specimen isn't suitable for exploring the effect of striated deformation on vibration resistance, later.

Then, due to the significant effect of heat treatment on the morphology of Sn-Pb eutectic solder, it can be applied to explore the size effect of microstructure. The stabilized Sn-40Pb specimens and Sn-40Pb C specimens, which were treated at 423K for 16 hrs to enlarge to grain size, were used in this subject.

D. The effect of striated deformation on vibration fracture resistance

Sn-Pb and lead-free Sn-Zn and Sn-Ag solders were used to explore to the effects of striated deformation on different alloy systems. Vibration testing was operated on an identical initial vibration amplitudes of 2.4 mm. The vibration conditions are given in Table 2.

III. Results and Discussion

A. The microstructure of Sn-Pb, Sn-Zn and Sn-Ag solders

Fig. 2(a)~(c) show the microstructural feature of stabilized Sn-Pb solders, where the darker regions are the Sn-rich phase and the lighter regions are the Pb-rich phase, that disperse like islands. The size and distribution of both phases are comparatively uniform in the near-eutectic Sn-40Pb sample (the average grain size is about 4.5 μm). As raised up Sn content, there are coarsely primary Sn-rich phase appear in Sn-30Pb samples. In addition, the average grain size of the Sn-40Pb C specimen could be enlarge to 8 μm after 423K × 16hrs treatment. The stabilized Sn-9Zn solder possesses the typical eutectic microstructure with needle-shaped Zn-rich

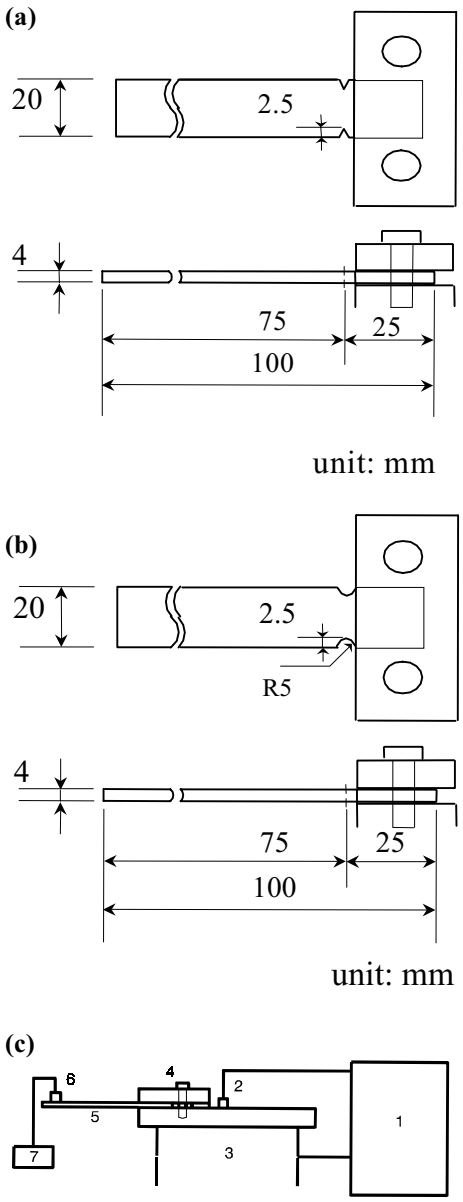

Figure 1 the dimension of the resonant vibration test specimen: (a) V-notched and (b) U-notched, and (c) a schematic of vibration equipment

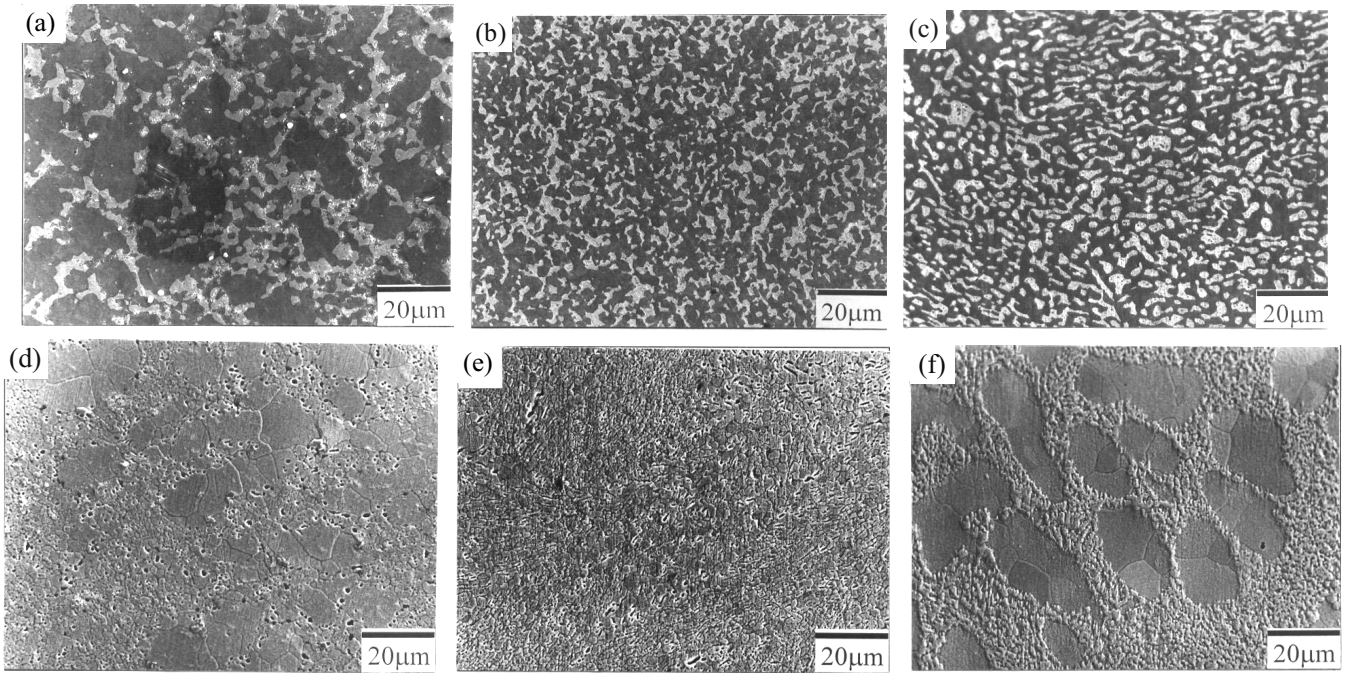

Figure 2 Microstructure of experimental materials in SEM: (a) Sn-30Pb, (b) Sn-34Pb, (c) Sn-40Pb C, (d) Sn-7Zn, (e) Sn-9Zn and (f) Sn-3.5Ag (Sn-Zn alloys and Sn-3.5Ag etched by 5% HCl)

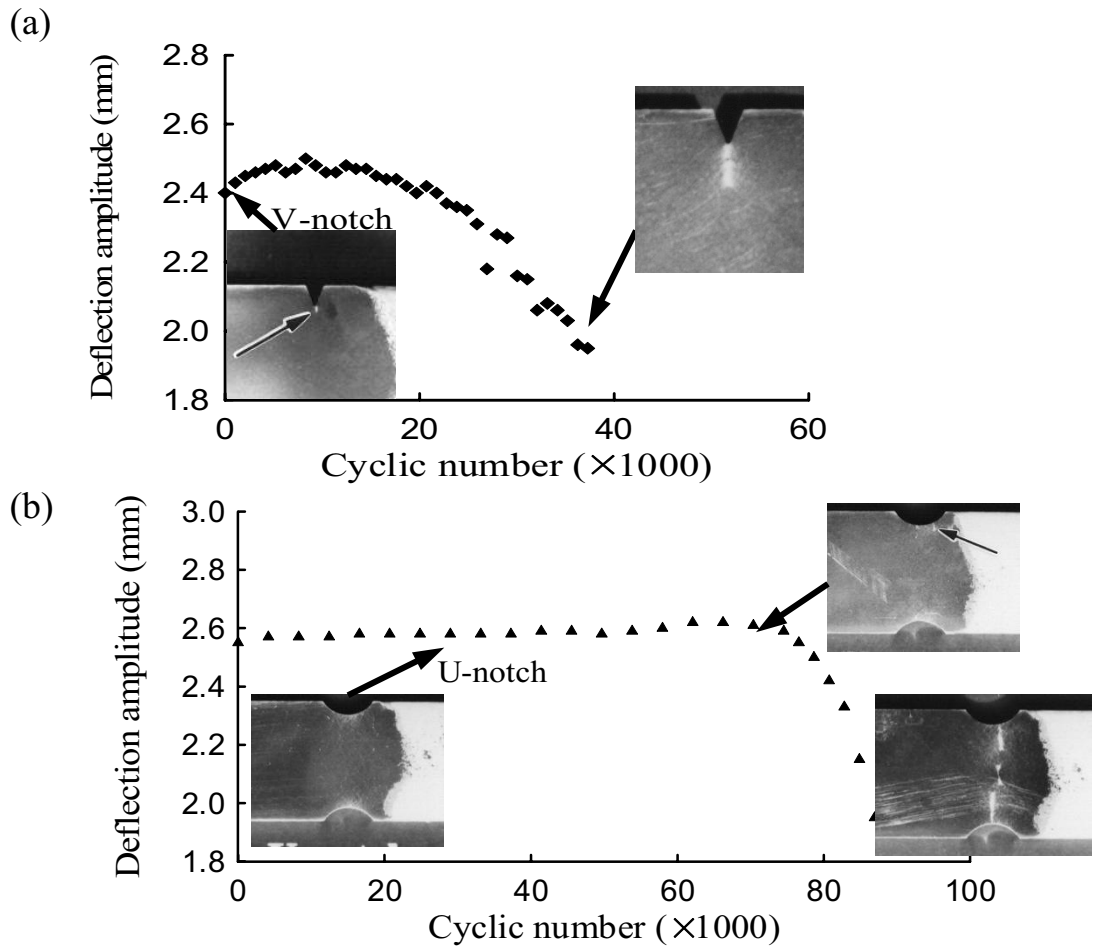

Figure 3 The D-N curves and surface observation of different notch-shaped specimens: (a) V-shaped notch, and (b) U-shaped notch

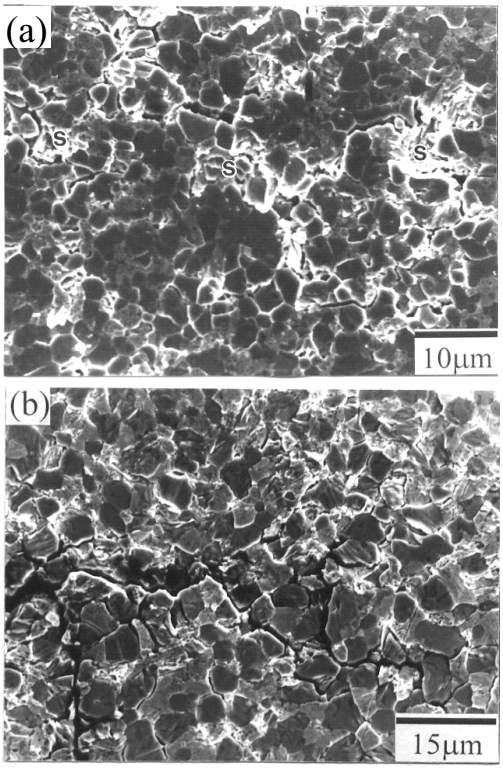

Figure 4 Sn-40Pb sample: (a) the striated deformation of U-notched specimen and (b) the surface observation of V-notched specimen

phase uniformly dispersed in Sn-rich matrix (Fig. 2(d)), while the primary Sn-rich phase appears dendritically in hypoeutectic Sn-7Zn (Fig. 2(e)). Besides, the morphology of Sn-3.5Ag also show the dendritic primary Sn-rich phase, and the second phase is composed by fine Ag_3Sn particles, that dispersed in eutectic areas (Fig. 2(f)).

B. The effect of number of cycles on the occurrence of striated deformation

The vibration testing results of Sn-40Pb specimens with different notched-shape were shown in Fig. 3. In V-notched specimen, the main crack appears and propagates from the initial vibration stage that leads to the shorter D-N curve. On the other hand, for U-notched specimen, the main crack occurs after a long cyclic number of vibration (when the D-N curve is near a drastic drop). Due to the initial stage of main crack is different between V-notched and U-notched specimens during vibration testing that makes the period of deflection amplitude keeping on resonant state is different. Fig. 4 shows the obviously different deformation behaviors on the two notched-shape specimen's surfaces after undergoing a certain cyclic number. In U-notched specimens, due to the specimen keeps a longer time on resonant state and the specimen's surface undergoes more vibration cycles, the striated deformation feature of Sn-rich phase was observed as shown in Fig. 4(a). However, the striated deformation didn't appear in V-notched specimen (Fig. 4(b)). Consequently, the onset condition of the occurrence of striated deformation can be corresponded to the number of cycles. The more integrative vibration cycles cause the striated deformation occurring easily under same grain size.

C. Size effect of microstructure on striated deformation

According to our pervious studies, the striated deformation only can be found in the matrix with coarse primary Sn-rich phase, that the critical onset condition apparently corresponded to the variation of grain size of Sn-rich phase. Based on the evidence obtained from the Sn-40Pb specimens with different grain size (stabilized Sn-40Pb: 4.5 μm, coarsen treated Sn-40Pb C: 8 μm), the striated deformation occurs in Sn-40Pb C sample but not in stabilized Sn-40Pb sample under an identical initial deflection (2.4mm) as shown in Fig. 4(b) and Fig. 5. The vibration test result shows that the D-N curve of Sn-40Pb C arrive is shorter, due to the striated deformation will cause the higher crack growth rate (Fig. 6). The above results show that the striated deformation feature appears easily in coarser Sn grains, due to the deformation resistance of larger grains is lower than smaller grains and dislocations move easily in larger grains to make obvious deformation feature.

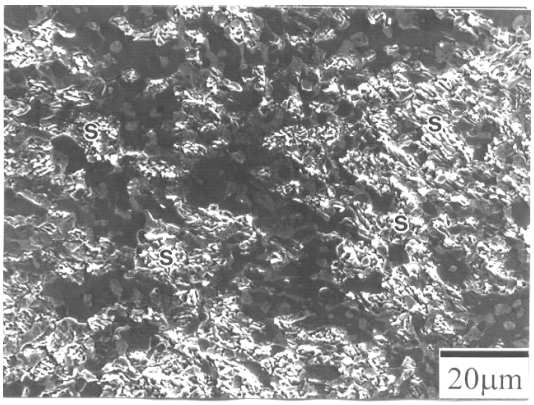

Figure 5 The striated deformation of Sn-40Pb C (grain size: 8 μm)

D. Effect of striated deformation on vibration fracture behavior between different microstructure

According to previous study[7~9], the longer D-N curve meaning better vibration resistance was defined. Fig. 7 and Fig. 8 depicted the vibration testing results of each alloy system respectively under an identical initial deflection amplitude of 2.4mm. In Sn-Pb system, the near eutectic Sn-40Pb possesses longer D-N curve (Fig. 7(a)) than hypoeutectic Sn-30Pb that result from higher crack propagation resistance (Fig. 8(a)). On the other hand, in the two lead-free solder systems, the longer D-N curves can be confirmed in Sn-7Zn and Sn-3.5Ag sample, that meaning the hypoeutectic microstructural materials posses better vibration resistance as shown in Fig. 7(b)(c) and Fig. 8(b)(c), oppositely. The observations of fracture appearance were shown in Fig. 9, the striated deformation appear in the primary Sn-rich phase of Sn-30Pb, Sn-7Zn and Sn-3.5Ag. In Sn-30Pb, there are many fine intergranular cracks accompany with observed striated deformation (Fig. 9(a)), and these fine cracks tend to link each other finally lead to the propagation of the main crack. The difference should be noted that very little micro-cracks can be observed around the striated deformation

regions of Sn-7Zn and Sn-3.5Ag samples (Fig. 9(b) and (c)), it can be considered that the striated deformation did not promote the main crack initiation and propagation. As observation above, the striated deformation plays different effect on the crack propagation between Sn-Pb and the two lead-free solder systems.

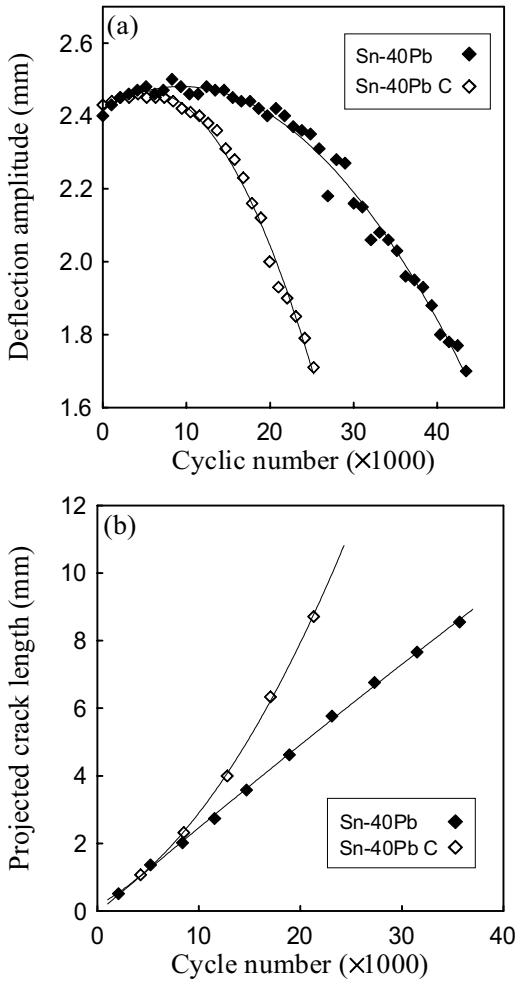

Fig. 6 The vibration results of different grain size of Sn-40Pb: (a) the D-N curve, and (b) the projected crack length versus vibration cycles

Schematic diagrams as shown in Fig. 10 and 11 help to explain the effect of the striated deformation that lead to induce micro-cracks or not in different microstructural alloy systems. In hypoeutectic Sn-30Pb sample, the interface is smoother among primary Sn-rich phase, neighboring eutectic Sn-rich phase and Pb-rich phase. When the striated deformation occurring in primary Sn-rich phase, the stress concentration will be induced in the triple point of phase boundary, that lead to the micro-crack initiation. The preexistence of micro-cracks will accelerate the propagation of main crack (Fig. 10). On the other hand, the microstructural features of Sn-7Zn and Sn-3.5Ag samples are significantly different from Sn-Pb solder, the eutectic phase in the surrounding of primary Sn-rich phase are formed by great amount of fine second phase particles. During vibration test, when the striated deformation was induced, these particles help to suppress the micro-crack initiation (Fig. 11). Hence, for Sn-7Zn and Sn-3.5Ag solders, the striated deformation phenomenon plays an important role of absorbing vibration energy to improve the vibration fracture resistance, inversely.

IV. Conclusions

1. The striated deformation of Sn-rich phase is common deformation phenomenon in Sn-solder alloys under vibration. The conditions of this deformation behavior can be related to the Sn grain size and vibration cycles. The coarser Sn phase and the more vibration cycles make the striated deformation occurring easily.
2. The striated deformation feature promotes the crack propagation rate in Sn-Pb solders, but it plays a absorbing energy role and ascents the vibration resistance in Sn-Zn and Sn-Ag solders.

Acknowledgments

This study was supported by a grant (NSC 89-2216-E-006-089) from the National Science Council of the Republic of China.

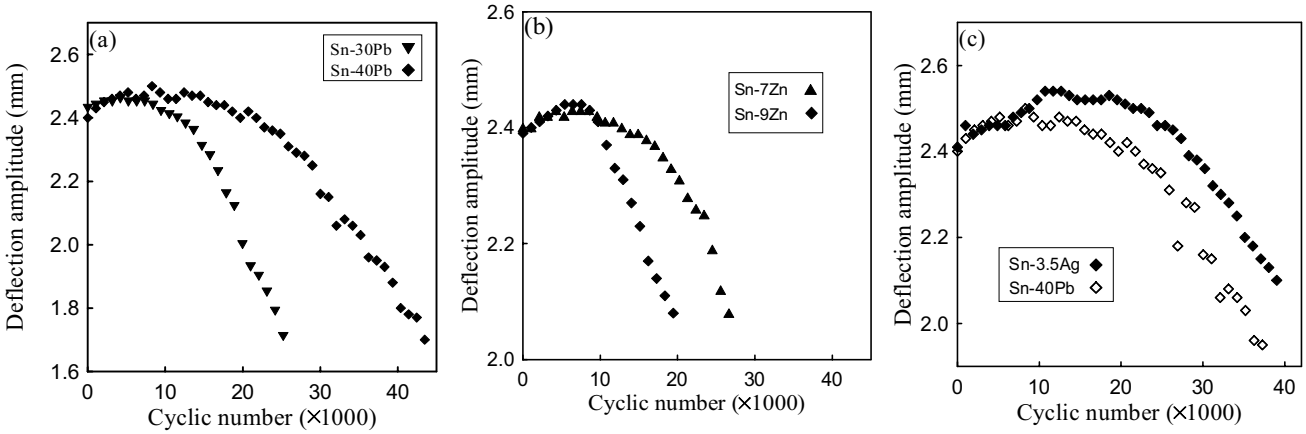

Figure 7 Deflection amplitude versus vibration cycles of (a) Sn-Pb solders, (b) Sn-Zn solders, and (c) Sn-40Pb and Sn-3.5Ag

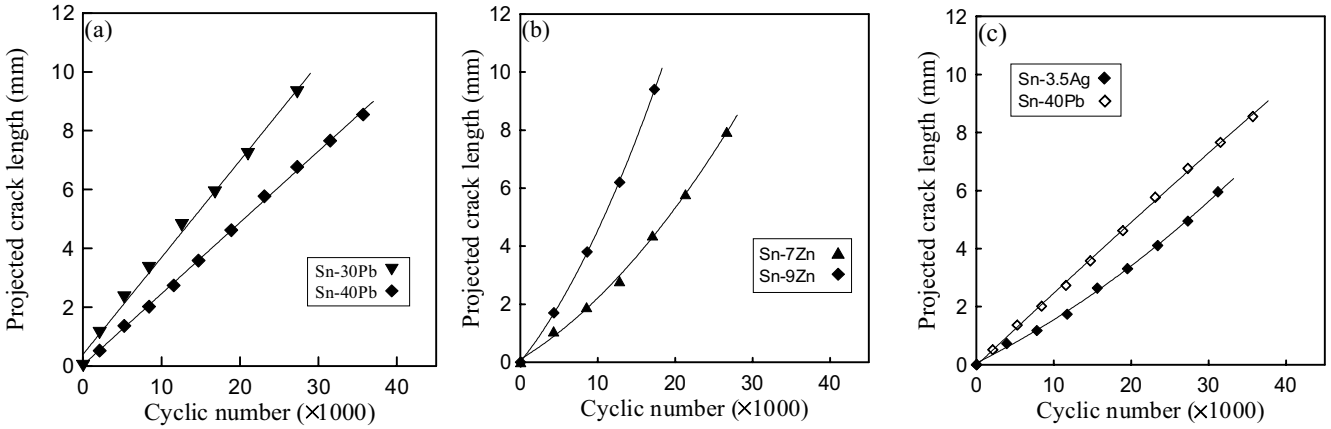

Figure 8 Projected crack length vs. vibration cycles of (a) Sn-Pb solders, (b) Sn-Zn solders, and (c) Sn-40Pb and Sn-3.5Ag

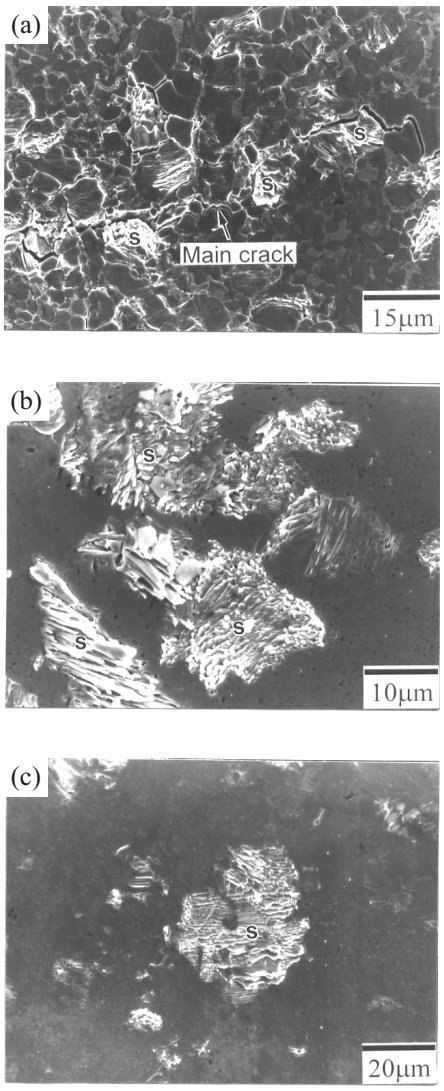

Figure 9 The striated deformation of Sn-rich phase in (a) Sn-30Pb, (b) Sn-7Zn, and (c) Sn-3.5Ag

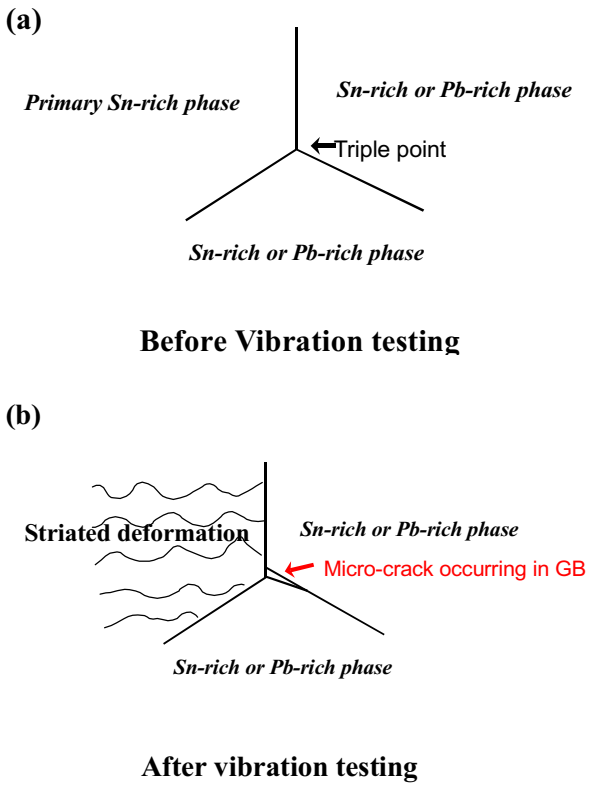

Figure 10 The mechanism of grain-boundary micro-cracks occurring in the surrounding of striated deformation (Sn-Pb system)

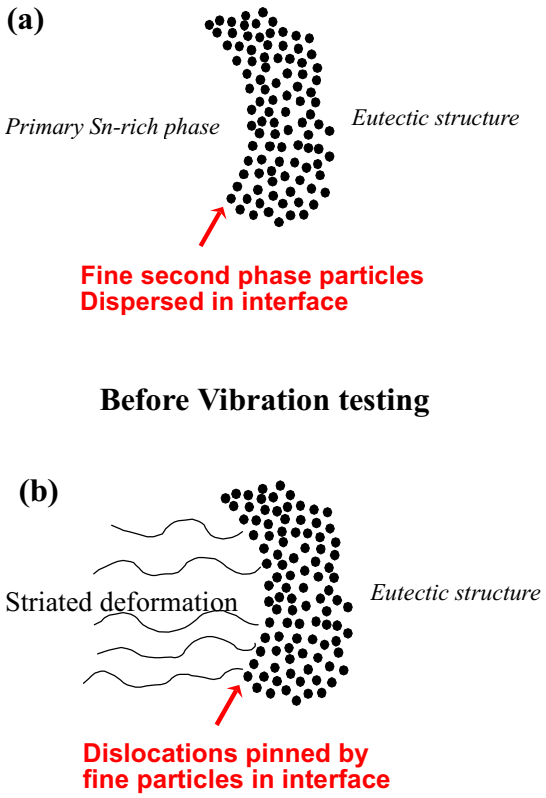

Figure 11 In Sn-Zn and Sn-Ag system, the second phase particles of interface around striated deformation will suppress the micro-crack initiation

References

1. B. Quintanilla-Vega, D. R. Smith, M. W. Kahng, J. M. Hernadez, A. Albores and B. A. Fowler, *Chemico-Biological Interactions*, Vol. 98 (1995), pp. 193-209.
2. V. N. Adonaylo and P. I. Oteiza, *Toxicology*, Vol. 135 (1999), pp. 77-85.
3. N.-C. Lee, *Soldering and Surface Mount Technology,* Vol. 26 (1997), pp. 65-68.
4. M. Mccormack, S. Jin and H. S. Chen, *J. Elec. Mater.,* Vol. 23 (1994), pp. 687-690.
5. S. M. McGuire, M. E. Fine, O. Buck and J. D. Achenbach, *J. Mater. Res.,* Vol. 8 (1993), pp. 2216-2223.
6. S. M. McGuire, M. E. Fine and J. D. Achenbach, *Metal. Trans A,.* Vol. 26A (1995), pp. 1123-1127.
7. C. M. Chuang, T. S. Lui and L. H. Chen, *J. Mater. Res*., Vol. 16, No. 9 (2001).
8. C. M. Chuang, T. S. Lui and L. H. Chen, *J. Elec. Mater.*, Vol. 30, No.9 (2001).
9. C. M. Chuang, T. S. Lui and L. H. Chen, *Mater. Trans., JIM,* Vol. 42, No. 10 (2001).

Reliability Evaluation of Semiconductor using Ultrasound

Hyoseong Jang[1], Job Ha[2], Kyungyoung Jhang[3], Joonhyun Lee[4]
[1]Sonix Korea, 1408 HanSeo BD, 11-11 Yoido-dong, Youngdungpo-gu, Seoul, Korea
[2]Department of Precision Mechanical Engineering
Graduate School of Hanyang University, Hangdang-dong 17, Seongdong- gu, Seoul 133-791, Korea
[3]School of Mechanical Engineeri`ng
Hanyang University, Hangdang-dong 17, Seongdong-gu, Seoul 133-791, Korea
[4]School of Mechanical Engineering
Pusan National University, Changjeon-dong 30, Keumjeong-ku, Pusan 609-735, Korea
E-mail: kyjhang@hanyang.ac.kr

Abstract

Recently, ultrasound has been a crucial non-destructive tool in the arsenial of semiconductor reliability evaluations and failure analysis. However, the semiconductor packaging industry is spending a great deal of time and effort developing thinner and thinner packages. Ultrasound works by measuring the amount of signal reflected from material interfaces. Thin packages create a potential problem because the resulant reflected signal from the die top and die attach layers an be nearly superimposed in the ultrasonic waveform. This makes it difficult to inspect for delaminations at the die attach adhesive interfaces.

Generally a preconditioning test is performed to evaluate reliability of semiconductor packages. This includes utilizing a Scanning Acoustic Microscope (SAM) at the beginning and end of the test to aid in the discovery of the existence of physical defects, such as like delaminations or package cracks. In particular and of primary concern are package cracks and delaminations caused by moisture being absorbed under ambient conditions. This moisture can lead to package cracks and delaminations during the reflow process by the volume expansion of moisture due to vaporatization.[1] This paper discusses the kind of failure mechanism associated with moisture absorption in plastic encapsulated semiconductors and the methodology of using SAMs to find failures such as cracks or delaminations grown during the preconditioning test.

Background

Up to now, semiconductors have been produced with a "productivity and quality first" mentality. Initial product quality was of primary interest. However, customers are becoming more concerned with the level of package quality throughout the lifetime of the package. Studying reliability variables such as durability, moisture, thermal shock, variation of temperature, are now given equal importance with “out-the-door” quality standards.

The preconditioning test is generally conducted to investigate whether initial quality satisfies these reliability variables. The preconditioning test is utilized throughout the manufacturing process until the product is soldered on a board. If a part fails anywhere during the process, it is essential to determine the cause of the fatal defect. Of primary importance during this testing is ensuring moisture absorption is not an on-going problem. That is to say, the main purpose of the reliability inspection process is to identify the effect of moisture sensitivity and therefore the extent of device durability. This requires the failure mechanism induced by moisture absorption in semiconductors to be well understood. SAM inspection has proven to be an effective tool in the investigation of the existence of moisture induced defects. Because the ultrasonic is method used with SAMs can determine most effectively not only the existence (or lack) of a defect in the finished good but also the defect pattern and properties.

Structure of the semiconductor

The internal structure of a semiconductor consists of a lead frame with a mounted silicon chip (micro chip) and typically gold bond wires to connect the circuit with the exterior. Epoxy Molding Compound (EMC) is used to protect all parts from the environment. Figure 1 demonstrates this structure.

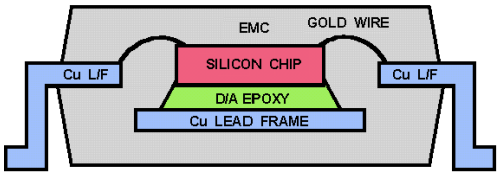

Fig. 1 Internal structure of a semiconductor

Using ultrasound for the evaluation of the reliability of semiconductors

The primary method for ultrasonic inspection of these types of devices involves pulse-echo or reflected mode techniques. This method allows for interface and depth specific information to be gleaned from the acoustic waveform. The density boundary between the EMC and the die, die and die attach and so on, also creates a boundary condition for acoustic impedance. Whenever an acoustic impedance mismatch in encountered, part of the ultrasonic signal gets reflected from the boundary and part is transmitted. The pulse-echo technique examines and measures only the reflected portion of the signal. By measuring the time interval between sound entering and leaving the sample, depth-specific data can be examined. The resultant image is called a C-Scan. Generating multiple C-scan images in one pass of the part, each at distinct depths within the sample is called a TAMI Scan. B-scans, a non-destructive cross-sectional image, also uses the reflected mode technique.

Through transmitted technique (T-scan) is a simple ultrasonic inspection method that measures transmitted sounds loss. Figure 2 shows a schematic diagram of a typical SAM

unit equipped to use either pulse-echo or T-scan techniques. [2]

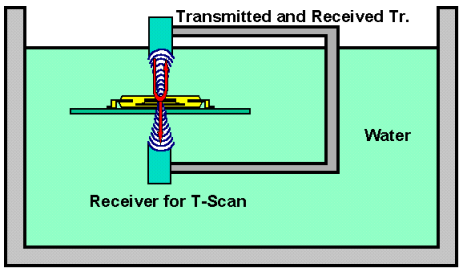

Fig. 2 Schematic diagram of a typical SAM

B-scan and C-scan

A B-scan, an image of the x-z or y-z plane, is an image that collects a returned signal's amplitude and propagation time from each interface within the device. Using the previously mentioned inspection method, the position, direction and depth of the defect can be accurately determined. Not only are defects observed, but also the shape of defect can be measure, which, up until now, we a difficult variable to study. The primary use of a B-scan image is to inspect devices for possible package cracks, die attach cracks, die tilt or EMC flaws.[3] Figure 3 shows an example B-scan image of a package crack induced by excessive moisture absorption.

A C-scan, an image of the x-y plane, is the most common acoustic image. C-scans are capable of showing the condition of a bonded surface by analyze the reflected wave's phase and amplitude. However, equipment settings, such as focusing the ultrasound, can make it difficult to determine the existence of package cracks by only examining the C-scan image. It is primarily used to inspect devices for delaminations at interfaces. Figure 4 shows an example of a C-scan image showing a delamination of the die surface.

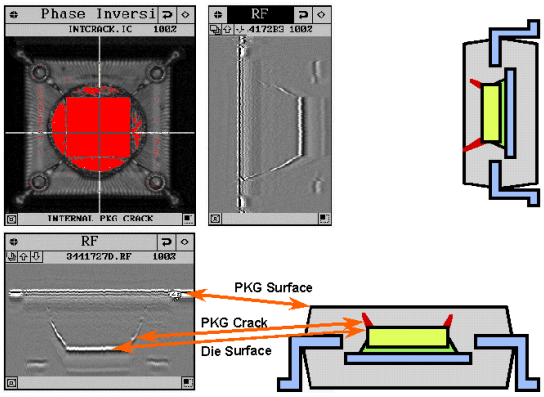

Fig. 3 B-scan image of plastic IC

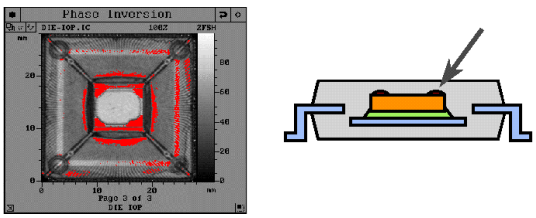

Fig. 4 C-Scan image of die surface

T-scan

Through transmission (or T-scan) imaging requires no special knowledge of the equipment, allowing an operator can easily inspect a test object in the easiest form. However, T-scan is limited in terms of the information the image can provide. Variables such as defect position and depth cannot be determined. For that reason, T-scan is mainly used as a quick "go/no go" inspection method. Figure 5 shows an example T-scan image. The right side of the device in this example is black because no sound propagates through the entire thickness of the device, indicating a delamination. However, the left side is gray indicating the area is well bonded.

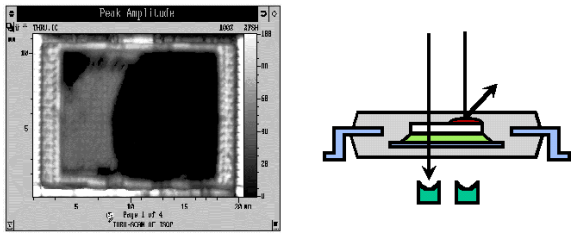

Fig. 5 T-scan image of a semiconductor

TAMI™ Scan

Tomographic Acoustic Micro Imaging (TAMI™) is one of the newest C-scan methods for seeing multiple layers within a semiconductor through utilization of a multi-gate method. Fully digital acoustic microscopes have the ability to generate many C-scan images with one scan of the device. Consequently, TAMI Scan helps resolve the conventional problem of focusing when performing C-scans because the operator can now quickly identify the area of interest. The name TAMI appropriately came from the medical term CAT (Computer Aided Tomography) Scan that is generally used for the diagnosis of the human body. A TAMI Scan acquires up to a maximum of 99 C-Scan images with a single scan of the device. The 99 C-Scan image "slices" can be evenly distributed through the entire thickness of the device. The minimum thickness of each slice corresponds to the equivalnet of one and a half times the wavelength of the transducer frequency used. TAMI Scans can accurately inspect almost every depth with the part in the same time it takes to perform a single scan (1-2 minutes. Not only can results be easily acquired but defects within the part can now be rendered three dimensions. Figure 6 shows an example of a TAMI Scan with 31 C-scan image slices.

Reliability evaluation of a semiconductor

To ensure adequate semiconducter reliability, the device must satisfy the following conditions…

(1) Moisture resistant.
(2) Heat resistant.
(3) Extreme temperature resistant.
(4) Well sealed. (internal exposure of the components to the outside environment is not tolerable)

Preconditioning testing involves the testing of all four of these conditions. A part failing any one of this criterium is a failed device. Preconditioning testing is perform through the production process until the component is soldered onto the end-product. This ensures initial component reliability. This test is usually accompanied with a series of other tests such as T/C Test (temperature cycling), T/S Test (thermal shock), HTST(high temperature storage), T&H Test(temperature and humidity), and PCT(pressure cooker). It is essential that the component passes each of these tests.

Through out these tests, a primary concern is moisture absorption. Moisture causes fatal defects such as crack or delamination in the package. If a defective component is mounted on a board, great expenses in incurring to discover the failed component and replace it. It is strongly preferred that defective components are culled from a lot as early in the production process as possible.

The extent of moisture absorption and the devices' ability to endure the moisture is one of the main goals during reliability evaluations. Scanning acoustic microscopes have previously been shown to be the best tool for this evaluation.[4]

Preconditioning test procedure

The process flow diagram for the peconditioning test is shown in Figure 7. Upon SAM inspection, defective samples are culled from the lot. Open/short testing and temperature cycle tests (-55/12 5°C, 5X) are carried out on assembled units to simulate the temperature variations commonly seen during transporation via airplanes. The test packages are subsequintly dry-baked at 125°C for 24 hours and then exposed to a temperature/humidity test (leve16) to model the degree of moisture absorption similar to the opening of the dry pack. The test packages are then exposed to IR or VPR(Vapor Phase Reflow) causing the condensed moisture to vaporize and delaminate at the weakest interface. Finally, SAM and open/short tester inspection is performed again in the final determination of which packages are acceptable.

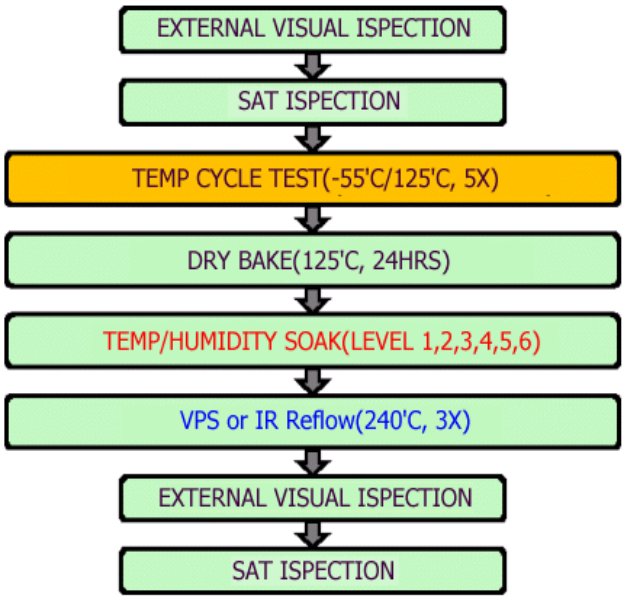

Fig. 7 Preconditioning test flow

The Temperature/humidity test is a very critical step in the reliability evaluation because it details not only initial product quality, but also indicates device lifetime. The purpose of this test is to estimate the lifetime of the component under certain temperature-humidity conditions. The outcome of this lifetime study is defined as the MSL(Moisture Sensitivity Level). The result is reported as a classificatiioin level and sould be used for initial reliability qualification. If initial reliability qualification exists and no major changes have been made, this test may be usde for reclassifiacation. The scaling of the MSL creteria is divided into 6 levels. If the rate is level 1, the IC is determinated to be good quality. The price of the manufactured good is based on the MSL rating. The standard package level is 3 at the present time, but an increasing

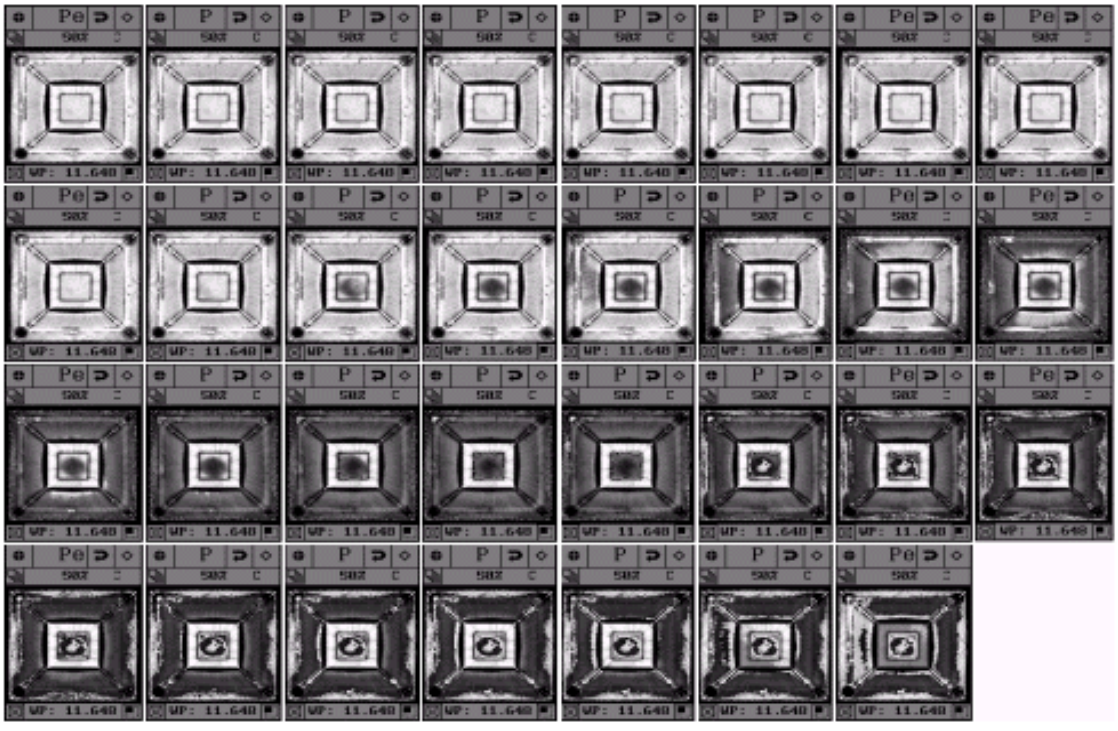

Fig. 6 Divided semiconductor into 31 equal parts by TAMI Scan

number of semiconductor customers are demanding level 1.

MSL Testing

Table 1 shows relation of temperature-humidity conditions to lifetime in the temperature-humidity test. Each MSL's absorption quantitiy has been satisfied with a standard lifetime when temperature-humidity conditions is shown in the middle column of Table 1. Lifetime after opening the waterproof packing can expect to correspond to results on the right column of Table 1.

Table 1. Moisture sensitivity level

LEVEL	TEMPERATURE/ HUMIDITY CONDITION (℃/%RH)	FLOOR LIFE
1	85/85, 168hours	Unlimited
2	85/60, 168hours	1 year
3	30/60, 192hours	168 hours (1 week)
4	30/60, 96hours	72 hours (3 days)
5	30/60, 72hours	48 hours (2 days)
6	30/60, 6hours	6 hours

Generally, weight gain analysis can be very valuable in determining the estimated shelf life of the device. Only one test device has to be used in this study. JEDEC J-STD-020A recommends ten devices be used in the sample so that the average weight can be calculated by simply moving the decimal place.[5] Percent weight gain measurements for the 85C°, 85%RH and 60%RH and 30C°, 60%RH conditions for test devices are shown in Figures 7 and 8. These conditions conform to levels 1, 2, 3 as shown in the above table. Also, in both of graphs, percent weight gain is proportional to the increase in the time of moisture absorption at the same lifetime condition. As a result, the temperature-humidity test can be an essential evaluation procedure in order to ensure reliability for the entire lifetime of the component

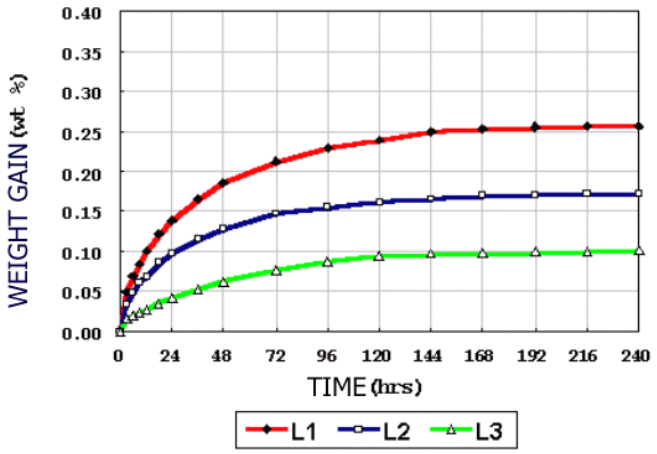

Fig. 7 Percent weight gain , condition:moisture absorption

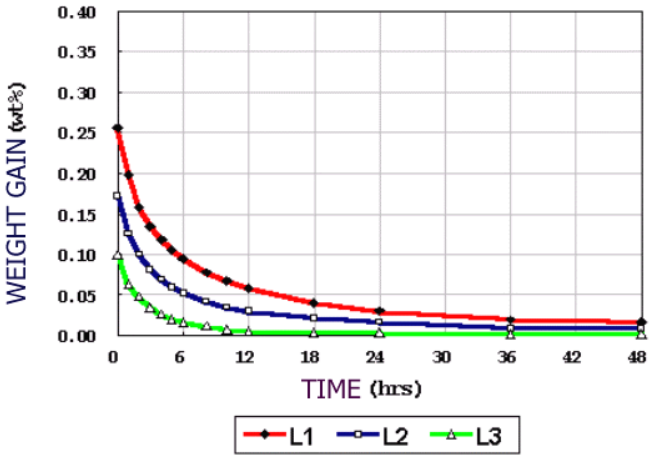

Fig. 8 Percent weight gain , condition:moisture desorption

Mechanism of a moisture induced defect

Moisture ingress in plastic molded packages has become a generic reliability issue that is now generally accepted as an industry wide problem. The mechanism of a moisture-induced defect has been shown to be caused by the phase change and expansion of internally condensed moisture in the package during exposure to solder reflow temperatures. That is to say, moisture inside a plastic package turns to vapor and expands 1,900 times in volume when the package is exposed to high temperature (240C°) seen during soldering onto a PCB. Fatal defects such as package cracks, delaminations and electric shorts between the EMC and lead frame is caused by the package instantaneously induced vaporization pressure. Other causes, such as a difference in the coefficient of thermal expansion (CTE) between materials, adhesive strength among the materials, and the cohesive force internal to the homogeneity of the material. Figure 9 shows a SEM photo of a package crack after defects in the preconditioning test were detected using ultrasound.

Defect inspection using ultrasound

The internal structure of the semiconductor is inspected using SAM before and after the preconditioning test. Firstly, the test before preconditioning sorts out defective parts included in sample lots. The post preconditioning test investigates what kinds of defects are caused by the test process.

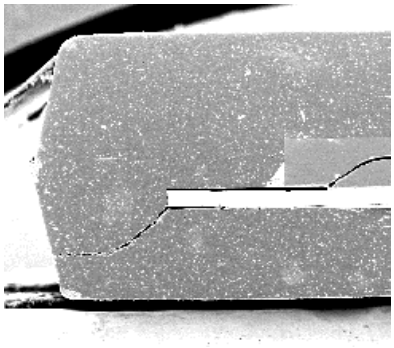

Fig. 9 Package crack caused by preconditioning test (SEM photo)

As mentioned above, there are four imaging techniques, B-scan, C-scan, TAMI Scan and T-scan, used to detect delaminations and cracks, etc. caused by the preconditioning test. Basically, SAM is a pulse-echo technique utilizing the reflection and transmission of high frequency ultrasonic waves. Images are acquired by scanning a focused transducer on the interfaces in packages. Also, SAM is a useful tool for helping determine the level of moisture sensitivity classification of the semiconductor packages. However, there is no "one-to-one" correlation between delamination and future electronic component failure or performance.

Fig. 10 shows the die top delamination image after reflow(260□C) produced by the scanning acoustic microscope. The red area in the image indicates delaminaiton caused during the preconditioning test.

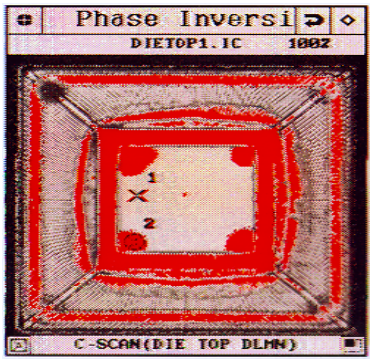

Fig. 10 Die top delamination, condition:260□C

In the process of the temperature-humidity test, an open defect can be easily caused by corrosion of the aluminium bonding pad being arsorbed through the epoxy mold compdound. In the pressure cooker test, just like in the temperature-humidity test, an open defect can be caused due to corrosion at the aluminium bonding pad passing through a gap between the EMC and lead frame. Corrosion testing was generally conducted using a combination of deliberate exposure to a common flux. The pressure cooker test images of a device for the 120°C, 100%RH, 504 hours and 2 ATM condition are shown in Figure 11.

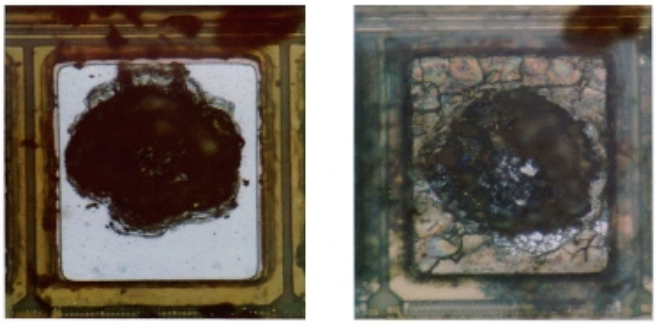

(a) No corrosion **(b) corrosion**

Fig. 11 Pad corrosion by PCT test

A critical cross-over point occurs when the strength of the plastic can no longer sustain the rising internal stresses generated by the expanding vapor and the resultant effect, in the worst case, is the rapid propagation of a package crack (commonly named to as a "Popcorn crack"). "Popcorn" cracks represent the worst case condition and are dependent on higher levels of moisture content, package/leadframe-die geometry, and molding compound/lead frame adhesion.

The optical microscope is a powerful tool for reliability evaluation but can not nondestructively see the inner parts of materials. Accordingly, nondestructive evaluation using the scanning acoustic microscope is a very useful reliability inspection technique. Figure 12 illustrates the advantages of the method using ultrasonics. Figure 12(a) and (b) were imaged by the optical microscop and by the scanning acoustic microscope, respectively, and Figure 12(c) compares the images of the optical microscope and the scanning acoustic microscope. The scanning acoustic microscope out-performs the optical microscope for reliability evaluations of semiconductors.

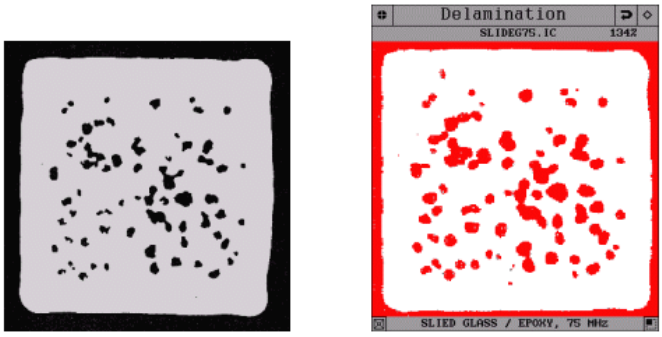

(a) Image by optical microscope **(b) Image by SAM**

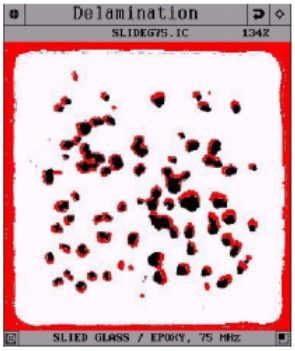

(c) Overlap image of optical microscope and SAM

Fig. 11 Comparison betweem optical microscope and SAM

Conclusions

The trend of the semiconductor manufacturing is making thinner and thinner packages because of the ease of integration and a high product speed. However, these new packages are susceptible to fatal defects such as delaminations and package cracks during the soldering process. Through effective usage of nondestructive inspection equipment, such a SAMs excellent reliability can be maintained. Integrating SAM equipment in the product qualification process is now required in order to satisfy customers increasing quality requirements. Improvements in SAM technology, such as high inspection

throughputs and reduced water exposure will increase the visibility of SAM equipment.

References

1. Lin R. et al, “Moisture Induced Package Cracking in Plastic Encapsulated Surface Mount Components During Solder Reflow Process”, Proc. 26th Rel. Phys. Sym.,1988, pp. 83-89.
2. Siettmann, J. et al, “Acoustic evaluation of electronic plastic packages”, Proc. 30th Rel. Phys. Sym.,1992, pp. 309-314.
3. Ishikawa, I. Et al, “Measurement of damaged layer thickness with reflective acoustic microscope”, IEEE Trans. Ultrasonics, Ferroelectrics and Frequency Control., Vol. 36, No. 6 (1989), pp. 587 –592.
4. Moore, T. M., “Identification of Plastic Defects in Plastic-Packaged Surface-Mount ICs by Scanning Acoustic Microscopy”, “Proc. Int. Sym. Testing & Failure Analysis, 1989, pp. 61-67.
5. Joint IPC/JEDE Standard J-STD-020A, “Moisture/Reflow Sensitivity Classification for Nonhermetic Solid State Surface Mount Devices”, 1999.

Study on Residual Stress in Viscoelastic Thin Film Using Curvature Measurement Method

Y. T. Im, J. H. Kim, and S. T. Choi
Korea Advanced Institute of Science and Technology
Department of Mechanical Engineering, ME3053, KAIST, Science Town, Daejeon, 305-701, Republic of Korea
Email: rookie9@kaist.ac.kr, Tel: +82-42-869-3053, Fax: +82-42-869-3095

Abstract

Using LSM (laser scanning method), the radius of curvature due to thermal deformation in polyimide film coated on Si substrate is measured. Since the polyimide film shows viscoelastic behavior, i.e., the modulus and deformation of the film vary with time and temperature, we estimate the relaxation modulus and the residual stresses of the polyimide film by measuring the radius of curvature and subsequently by performing viscoelastic analysis. The residual stresses relax by an amount of 10 % at 100 ^{o}C and 20 % at 150 ^{o}C for two hours.

1. Introduction

In electronic devices or MEMS (micro-electro mechanical system) devices, polyimide films are widely used as dielectric layers because of their excellent thermal stability, good mechanical properties, and low dielectric constant. Thermal deformation due to CTE (coefficient of thermal expansion) mismatch between polyimide and silicon takes place when the polyimide film/Si is cooled down to a room temperature after being coated on Si substrate at high temperature, and this thermal deformation results in thermal stress in the system. The thermal deformation and the induced thermal stress have negative effects on the manufacturing process and sometimes cause the system to fail. Therefore, the measurement of the thermal deformation is important for evaluating the reliability of film/substrate structures.

Various methods for measuring the residual stresses in film/substrate structures have been developed. For example, X-ray diffraction method, Raman method, and curvature measurement method using optical interferometry or laser scanning can be found in the literature [1-6]. X-ray diffraction method detects the change of lattice spacing due to the occurrence of strains [2]. Since X-rays usually penetrate multilayers deeply, not only strains but also the information about yielding, cracking, and delamination in the individual layers can be examined. But this method is available only for crystalline materials. Laser Raman spectroscopy deals with the measurement of the radiation scattered from a solid, liquid, or gaseous sample [3]. The characteristic peak in wave spectrum determined by interatomic force is shifted by the change of interatomic distance due to residual stresses. However, to quantify residual stresses, this method requires the standard shift of the characteristic peak obtained from the hydrostatic pressure experiments. In curvature measurement method using optical interferometry [4], a simple count of interference fringes permits the determination of curvature. Another effective method of curvature measurement is to use laser-scanning technique, which is based on the principle that a laser beam reflected on a curved surface depends on the orientation of the surface. Flinn et al. [5] have developed a laser-scanning device that makes use of a rotating mirror to scan the laser beam over a curved surface. In this study, LSM using a translating mirror instead of a rotating mirror is designed to control a laser beam entering the specimen surface.

Analyses of residual stresses in multilayered structures have been performed by many researchers. Stoney [7] proposed a simple formula known as Stoney's formula for the radius of curvature and the residual stress of a film/substrate system. This formula is applicable when the thickness of film is less than 1/20 of that of substrate. By using the continuity of strain at the interface between substrate and film, Timoshenko [8] analyzed thin films on a thick substrate. His analysis can take into account the effect of the thickness of films, but cannot be used for multilayered structures having different histories of temperature for each layer. CBA (composite beam analysis) has been developed by Lim et al. [9] for multilayered structures by means of cut and paste scheme. In CBA, the effect of the thickness of each layer is taken into account and multilayered structures having different histories of temperature for each layer can also be analyzed. These elastic analyses are also useful for materials having viscoelastic properties if the elastic-viscoelastic correspondence principle is valid. In this study, to estimate the relaxation modulus and the stress relaxation in polyimide film, the radius of curvature measured by LSM is analyzed with Stoney's formula and the correspondence principle.

2. Experimental Background

In this section, we briefly review the fundamentals of LSM, Stoney's formula for film/substrate structures, and the theory of viscoelasticity. LSM makes use of the fact that the direction of laser beam deflected on a specimen surface is dependent on the curvature of the surface. Referring to the geometric relations depicted in Fig. 1, the law of deflection [10], that the angle between an incident laser and a specimen surface equals the angle between the reflected laser and the surface, yields

$$\Delta d = \Delta x + L\left(\theta_1 + 2\theta\right) - L\theta_1 \cong \Delta x + 2L\frac{\Delta x}{R}, \qquad (1)$$

in which the translation of laser beam in x-direction, Δx, is assumed to be very small enough to have $\Delta x = R\theta$. Then, eq. (1) gives us the radius of curvature in terms of Δx, Δd, and L as follows:

$$R = \frac{2\Delta x}{\Delta d - \Delta x} L. \qquad (2)$$

Residual stress in thin film bonded on a relatively thick substrate was obtained by Stoney [7]. Thermal deformation due to CTE mismatch, $\Delta\alpha = \alpha_f - \alpha_s$, where α_f and α_s are CTE of the film and the substrate, respectively, is related to the radius of curvature and the residual stress, σ_f, as follows:

$$\frac{1}{R} = \frac{6M_f h_f}{M_s h_s^2}\Delta\alpha\Delta T\,, \tag{3}$$

$$\sigma_f = M_f \Delta\alpha\Delta T = \frac{M_f h_s^2}{6Rh_f}, \tag{4}$$

where ΔT is the temperature excursion. Hereafter, the subscripts s and f refer to the substrate and the film, respectively. $M_f = E_f/(1-\nu_f)$ is the biaxial modulus of the film, where E_f and ν_f are Young's modulus and Poisson's ratio of the film, respectively. For the case of cubic crystals, we found that the biaxial modulus of the substrate is $M_s = \left(c_{11}^2 + c_{11}c_{12} - 2c_{12}^2\right)/c_{11}$, where c_{11} and c_{12} are the anisotropic elastic constants of the cubic crystals. It should be noted that the residual stress due to the thermal deformation in the film/substrate structure is the biaxial stress state, even though the substrate has cubic symmetry. Stoney's eq. (3) is applicable when the film thickness, h_f, is less than 1/20 of the substrate thickness, h_s, and the film and the substrate are linear elastic [1].

Polymeric materials like polyimide usually have viscoelastic behavior at elevated temperature [11], which may be described by viscoelastic constitutive relation,

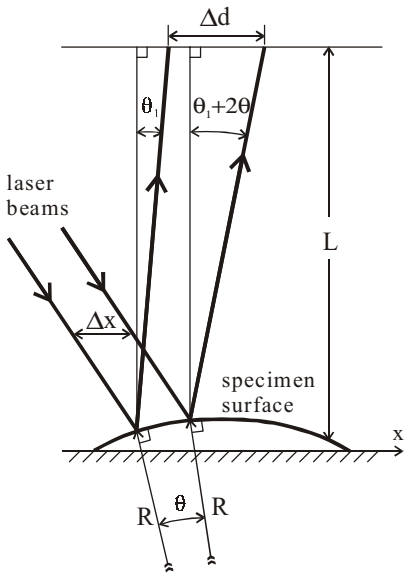

Fig. 1 Geometric relations of laser beams reflected on a specimen surface.

$$\sigma(t;T) = \int_0^t M\ (t-\tau;T)\frac{d\varepsilon(\tau)}{d\tau}d\tau\,, \tag{5}$$

for biaxial stress state, where $\sigma(t)$ and $\varepsilon(t)$ are the biaxial stress and strain, respectively. While the stresses are being relaxed, the temperature field is assumed to be constant and uniform. The basic postulate of thermorheologically simple material [12], which the polyimide film is assumed to be, is

$$M_f(t;T) = M_f\left[t\chi(T)\right], \tag{6}$$

in which the shift function, $\chi(T)$, should be determined experimentally. The meaning of eq. (6) is that the changes in temperature cause the relaxation function to be shifted to the right or left when plotted against $\log t$, as abscissa. With the elastic-viscoelastic correspondence principle [12], the radius of curvature and the residual stress in eqs. (3) and (4) for elastic film/substrate structures can be converted to Laplace-transformed viscoelastic solutions, of which inverse transform gives us

$$\frac{1}{R(t;T)} = \frac{6M_f\left[t\chi(T)\right]h_f}{M_s h_s^2}\Delta\alpha\Delta T\,, \tag{7}$$

$$\sigma_f(t;T) = M_f\left[t\chi(T)\right]\Delta\alpha\Delta T = \frac{M_s h_s^2}{6h_f}\frac{1}{R(t;T)} \tag{8}$$

for a given ΔT (ΔT is the temperature jump at $t = 0$).

3. Experiment

Specimen preparation

Thermoplastic polyimide is spin-coated on p-type (100) silicon wafer with 400-μm thickness and 3-inch diameter. Polyimide is a common dielectric, of which glass transition temperature, T_g = 400 °C, is high enough to stand the process of metal depositions. Polished silicon wafer on which polyimide solution has been put is rotated with 1000 rpm for 10 seconds and 1800 rpm for 30 seconds. The solvent of the coated polyimide solution is removed under 250 °C / 1 hr / vacuum condition. Then we get 15 μm-thick polyimide film on silicon substrate, which is assumed to be in stress-free state at T_m = 250 °C.

Curvature measurement using LSM

LSM using translating mirror is adopted to measure the radius of curvature as shown in Fig. 2. Since LSM is limited to specimens having a mirror surface, laser beams scan the silicon surface of the polyimide/Si specimen, instead of the polyimide surface. The translational displacement in x-direction instead of the angle of the mirror is controlled by the translation stage. With the linear encoder, the translational displacement, Δx, can be measured within 0.5 μm resolution. The laser beam reflected on the specimen surface enters PSD (position sensitive photodetector), which can detect the

translation, Δd , in x-direction of the reflected laser beam. By using eq. (2), the radius of curvature of the specimen is measured. The resolution of PSD is 0.15 μm and the distance, L , between PSD and the specimen is 0.85 m. Since $\Delta d - \Delta x$ cannot be less than the resolution of PSD, the maximum radius of curvature measurable with the apparatus shown in Fig. 2 is 2.27 km for Δx = 200 μm, which corresponds to 1.28-μm deflection at the center of the specimen with 3-inch diameter. The error in measuring the radius of curvature is expected to be less than 5 %.

Viscoelastic property measurement

Relaxation moduli of the polyimide are functions of time and temperature as described in section 2. The standard linear solid model [13] is introduced for the polyimide film to get

$$E_f(t;T) = E_\infty + E_0 \exp\left[-\frac{t}{\tau}\chi(T)\right] \tag{9}$$

with ν_f = 0.4 [9]. The arrows in the temperature-time graph of Fig. 3(a) denote the history of temperature which the specimens manufactured at T_m = 250 °C experience. The prepared specimens are maintained at T_h = 150 °C (or 100 °C) in a temperature chamber, except only for each of about 5 minutes at t = 0, t_1, t_2, ⋯, which are the time spent to measure the radius of curvature at room temperature, T_r = 20 °C. The time intervals, $\Delta t_i = t_i - t_{i-1}$, between each measurements are chosen to be about 2~4 hours. Since the stress relaxation hardly occurs at room temperature and moreover, the 5-minute interruption (time spent to measure) at T_r = 20 °C is very small compared to the time constant, τ , of the relaxation modulus (as confirmed in section 4), each 5 minutes at t = 0, t_1, t_2, ⋯ are ignored, i.e., each 5 minutes are assumed to have no effect on the stress relaxations at the elevated temperature. At t = 0, the elastic constant, $E_f(0)$, is only estimated with eq. (3) by measuring the radius of curvature at room temperature corresponding to the point, R_0 , instead of H_0 in Fig. 3(b), where $\Delta T_r = T_m - T_r$ and $\Delta T_h = T_m - T_h$. Subsequent measured values of the radii of curvature at $t = t_1$, t_2, t_3 correspond to the residual stresses at the points, R_1, R_2, R_3 on the dotted line in Fig. 3(b). To evaluate stress relaxation curve at T_h , a solid line in Fig. 3(b), the amount of $M_f(0)\Delta\alpha(T_h - T_r)$ corresponding to the length of the vertical lines between R_i 's and H_i 's ($i = 0,1,2,\cdots$) in Fig. 3(b) should be subtracted in the obtained residual stresses.

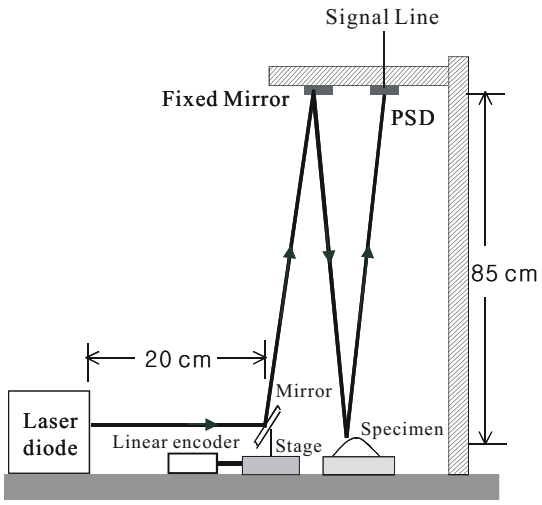

Fig. 2 Schematic diagram of experimental apparatus.

4. Results and Discussion

Experiment has been performed for 3 polyimide/Si specimens prepared according to the procedure described in section 3. Laser scanning is carried out on the diameter of Si wafer running to $\langle 011 \rangle$ direction for all specimens. Since the specimens are in the biaxial stress state, all the radii of curvature must be independent of measuring directions on the specimen surfaces. Since the thickness ratio of the polyimide film and the Si substrate used in our experiment is

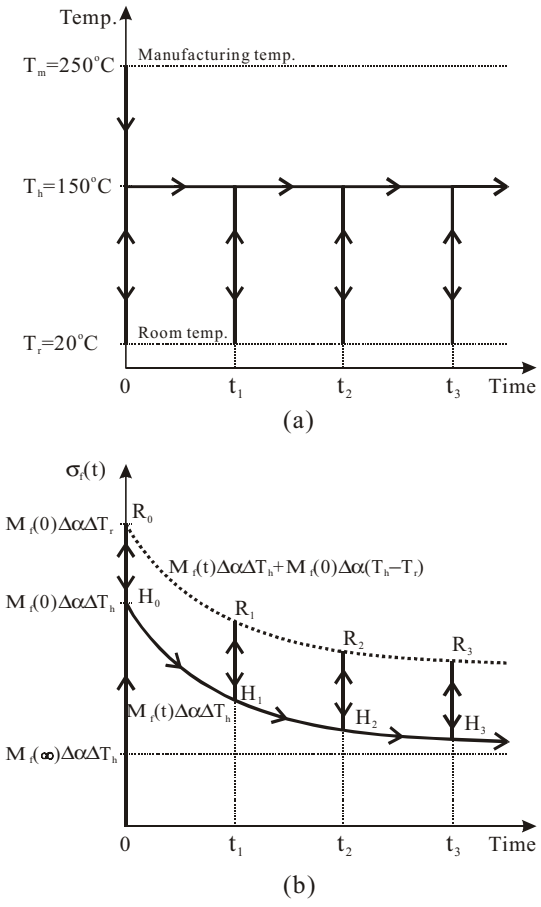

Fig. 3 Temperature profile (a) and results of the measurement of residual stresses (b).

$h_f/h_s = 3/80$, Stoney's formulae, eqs. (3) and (4), and the viscoelastic solutions, eqs. (7) and (8), obtained by applying the correspondence principle to Stoney's formulae are valid. The material properties of Si are c_{11} = 165.7 GPa, c_{12} = 63.9 GPa, c_{44} = 79.6 GPa, and α_s = 2.6 ppm/ ^{o}C [9, 14]. The CTE of the polyimide film is α_s = 40 ppm/ ^{o}C [9], which is assumed to be constant below the glass transition temperature. Relaxation modulus of the polyimide film are measured, as described below.

Thermal deformation at room temperature and t = 0

Single crystalline silicon wafers usually have not only surface roughness but also surface curvature after polishing. Before coating a polyimide film on Si substrate, the radius of curvature of polished silicon surface is measured in order to investigate the pure effect of the thermal deformation. The relation below is used:

$$\frac{1}{R_t} = \frac{1}{R_a} - \frac{1}{R_b}, \qquad (10)$$

in which R_b and R_a are the measured radii of curvature before and after coating, respectively, and R_t is the radius of curvature purely due to thermal deformation (Table 1).

Table 1 Measured values of radius of curvature, Young's modulus, and residual stress at room temperature and $t = 0$.

Specimen no.	# 1	# 2	# 3	**Avg.**
R_b (m)	85.0	56.7	34.0	—
R_t (m)	20.6	19.5	17.4	**19.2**
E_f (GPa)	1.09	1.15	1.29	**1.18**
σ_f (MPa)	15.6	16.5	18.5	**16.9**

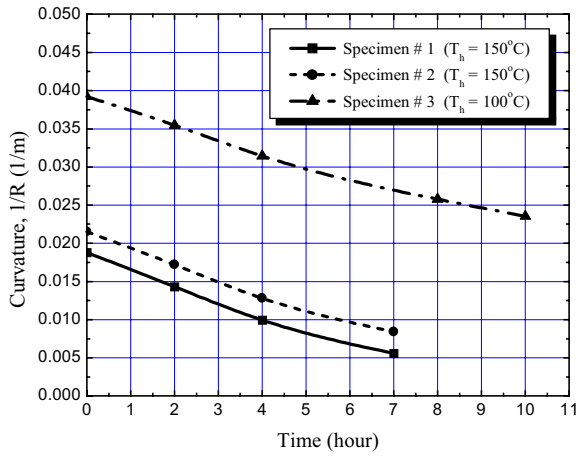

Fig. 4 Measured values of curvature depend on time and temperature due to the stress relaxation.

Young's modulus, $E_f(0;T)$, (assumed to be temperature independent as in eq. (9)) and the residual stress, $\sigma_f(0;T)$, of the polyimide film at room temperature are calculated by eqs. (7) and (8) with $E_f(0;T) = M_f(0;T)(1-\nu_f)$, ΔT = 230 ^{o}C, and ν_f = 0.4. The averaged Young's modulus and residual stress are $E_f(0;T)$ = 1.18 GPa and $\sigma_f(0;T)$ = 16.9 MPa, respectively, as given in Table 1. Since the stress relaxation hardly occurs at room temperature, we set $\chi(T_r = 20^o C) = 0$, which gives us that $E_f(t;T_r)$ = 1.18 GPa and $\sigma_f(t;T_r)$ = 16.9 MPa are constant, regardless of the elapsed time.

Curvature, relaxation modulus, and stress relaxation at elevated temperature and t ≠ 0

The curvatures of two specimens (#1 and #2) maintained at 150 ^{o}C and one (#3) at 100 ^{o}C, respectively, are measured and plotted against time in Fig. 4. The curvature of the specimen #3 is larger than those of the specimens #1 and #2, which means that the residual stress in the specimen #3 is larger that those in the specimens #1 and #2. As time elapses, the curvatures exponentially decrease, which corresponds to the stress relaxation. With the graph of the measured curvatures vs. time (Fig. 4) and the standard linear solid model, eq. (9), the relaxation modulus of the polyimide film is curve-fitted to be

$$E_f(t;T) = 0.2207 + 0.9593\exp\left[-\frac{t\chi(T)}{5.08}\right] \text{ (GPa)} \qquad (11)$$

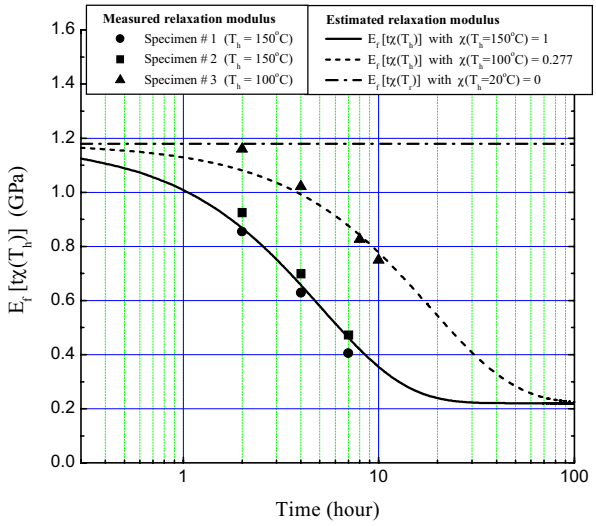

Fig. 5 Relaxation modulus of the polyimide film is estimated by the measured values to be $E_f(t;T) = 0.2207 + 0.9593\exp\left[-t\chi(T)/5.08\ hr.\right]$ together with the values of the shift function, $\chi(T)$ = 0, 0.227, and 1, at T = 20 ^{o}C, 100 ^{o}C, and 150 ^{o}C, respectively.

together with the values of the shift function, $\chi(T) = 0$, 0.227, and 1, at $T = 20$ °C, 100 °C, and 150 °C, respectively (Fig. 5). In fitting the curve, we choose $\chi(T) = 1$ at $T = 150$ °C. The time constant of the relaxation modulus, eq. (11), is $\tau = 5.08$ hour, which is large enough to ignore the 5-minute interruptions spent to measure the radius of curvature. At $t = 0$, $E_f(0;T) = 1.18$ GPa regardless of temperature. As time goes to infinity, $E_f(t;T)$ approaches $E_\infty = 0.2207$ GPa. In Fig. 5, if the relaxation function for $T_h = 100$ °C is shifted to the left by an amount of $\left|\log \chi(100\ ^\circ\mathrm{C})\right| = 0.652$, the relaxation function for $T_h = 100$ °C coincides with that for $T_h = 150$ °C. The residual stresses are also calculated by the obtained relaxation modulus, eq. (11), and eq. (8), $\sigma_f(t;T) = M_f\left[t\chi(T)\right]\Delta\alpha\Delta T$, where the biaxial modulus is related to the relaxation modulus by $M_f(t;T) = E_f(t;T)/(1-\nu_f)$ (Fig. 6). The dotted and broken horizontal lines in Fig. 6 denote the residual stresses at $T_h = 100$ °C and $T_h = 150$ °C, respectively (at $t = 0$), which are simply $M_f(0)\Delta\alpha\Delta T_h$. Since the temperature jump, $\Delta T_h = T_m - T_h$, for $T_h = 100$ °C is larger than that for $T_h = 150$ °C, the residual stress at 100 °C is larger than that at 150 °C, and the stress relaxation at 150 °C takes place faster than at 100 °C. It relaxes by an amount of 10 % at 100 °C and 20 % at 150 °C for two hours after manufacturing. As time goes to infinity, the residual stress approaches $M_f(\infty)\Delta\alpha\Delta T_h$. Were it not for the viscoelastic effect of the polyimide film, the residual stresses would be overestimated by the amount of $\left[M_f(0) - M_f(\infty)\right]\Delta\alpha\Delta T_h$, which corresponds to about 80 % of the residual stresses at $t = 0$.

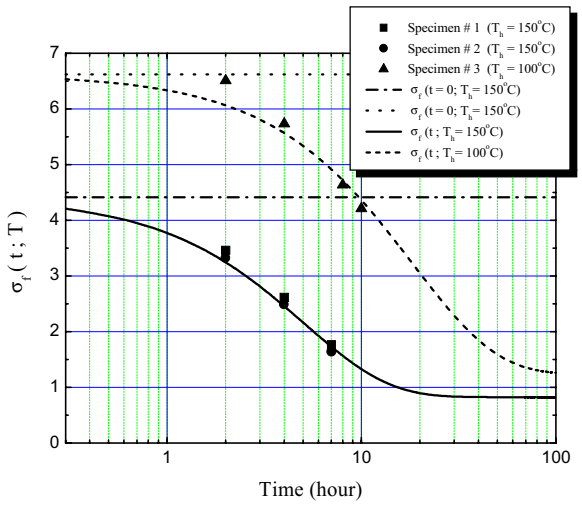

Fig. 6 Residual stresses due to CTE mismatch at $T_h = 100$ °C and 150 °C.

5. Conclusions

Experimental apparatus using LSM is developed for measuring the radius of curvature due to the thermal deformation in polyimide film coated on Si substrate. The system is capable of detecting the radius of curvature up to about 2.27 km. This LSM is limited to specimens having a mirror surface. After manufacturing the polyimide/Si specimens at 250 °C, the specimens are maintained at elevated temperature, $T_h = 150$ °C (or 100 °C). Relaxation modulus and stress relaxation in the polyimide film are estimated by measuring the values of the radius of curvature at an interval of about 2 hours, and then, by performing the viscoelastic analysis, which is based on the elastic-viscoelastic correspondence principle. At room temperature, the stress relaxation hardly occurs and Young's modulus of the polyimide film is obtained to be $E_f = 1.18$ GPa. The residual stresses relax by an amount of 10 % at 100 °C and 20 % at 150 °C for two hours after manufacturing.

Acknowledgments

This work has been supported by Computer Aided Reliability Evaluation (CARE) for Electronic Packaging: National Research Laboratory (NRL) program.

References

1. Nix, W. D., "Mechanical Properties of Thin Films," Metal. Trans. A, Vol. 20A (1989), pp. 2217-2245.
2. Kämpfe, B., "Investigation of Residual Stresses in Microsystems Using X-ray Diffraction," *Material Science and Engineering*, Vol. A288 (2000), pp. 119-125.
3. Laserna, J. J., Mordern Techniques in Raman Spectroscopy, John Wiley & Sons (Spain, 1996).
4. Courjon, D. *et al*, "New Optical Near Field Developments: Some Perspectives in Interferometry," Ultramicroscopy, Vol. 61 (1995), pp. 117-125.
5. Flinn, P. A. *et al*, "Measurement and Interpretation of Stress in Aluminum-Based Metallization as a Function of Thermal History," *IEEE Trans. on Electronic Devices*, Vol. ED-34, No. 3 (1987), pp. 689-699.
6. Witvrouw, A. *et al*, "Determination of the Plane Stress Elastic Constants of Thin Films from Substrate Curvature Measurements: Applications to Amorphous Metals," J. Appl. Phys., Vol. 73 (1993), pp. 7344-7350.
7. Stoney, G. G., "The Tension of Metallic Films Deposited by Electrolysis," *Proc. Royal Soc.*, Vol. A82 (1909), pp. 172-175.
8. Timoshenko, S., "Analysis of Bimaterial Themostats," *J. Opt. Soc. Am.*, Vol. 11 (1925), pp. 233-256.
9. Lim, J. H. *et al*, "A Thermomechanical Analysis of MCM-D Substrate of Polymer and Metal Multilayer," *Key Engineering Materials*, Vol. 183-187 (2000), pp. 1123-1128.
10. Hecht, E., Optics, Addison-Wesley (1998).
11. Findley, W. N. *et al*, Creep and Relaxation of Nonlinear Viscoelastic Materials with an Introduction to Linear

Viscoelasticity, North Holland Publishing Company (Oxford, 1976).
12. Christensen, R. M., Theory of Viscoelasticity, Academic Press (1982).
13. Ward, I. M. *et al*, An Introduction to the Mechanical Properties of Solid Polymers, John Wiley & Sons (1993).
14. Suwito, W. et al, "Elastic Moduli, Strength, and Fracture Initiation at Sharp Notches in Etched Single Crystal Silicon Microstructures," J. Appl. Phys., Vol. 85 (1999), pp. 3519-3534.